Nanoscale

Accepted Manuscript

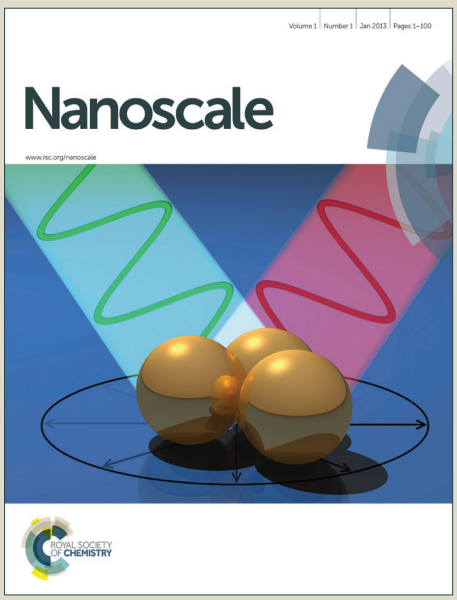

ROYAL SOCIETY OF CHEMISTRY

www.rsc.org/nanoscale

Journal Name

RSCPublishing

ARTICLE

Metal-organic frameworks derived Fe_2O_3@$NiCo_2O_4$ porous nanocages as anode materials for Li-ion batteries

Cite this: DOI: 10.1039/xoxxoooooox

Received ooth January 2012,
Accepted ooth January 2012

DOI: 10.1039/xoxxoooooox

www.rsc.org/

Gang Huang[ac], Leilei Zhang[ac], Feifei Zhang[ac] and Limin Wang[ab]*

Metal-organic frameworks (MOFs) with high surface areas and uniform microporous have showed potential applications in many fields. Here we report a facial strategy to synthesize Fe_2O_3@$NiCo_2O_4$ porous nanocages by annealing core-shell $Co_3[Fe(CN)_6]_2$@$Ni_3[Co(CN)_6]_2$ nanocubes under air. The obtained samples have been systematically characterized by XRD, SEM, TEM and N_2 adsorption-desorption. The results show that the Fe_2O_3@$NiCo_2O_4$ porous nanocages have an average diameter of 213 nm and the shell thickness is about 30 nm. As anode materials for Li-ion batteries, the Fe_2O_3@$NiCo_2O_4$ porous nanocages exhibit a high initial discharge capacity of 1311.4 mAh g^{-1} at current density of 100 mA g^{-1}(about 0.1 C), and the capacity still retains at 1079.6 mAh g^{-1} after 100 cycles. The synergistic effect of different components and the porous hollow structure may contribute to the outstanding performance of the composite electrode.

Introduction

Since lithium ion batteries (LIBs) introduced into market, the commercialized targets have extended from small mobile devices such as camcorders, cell phones, laptops and power banks, to large-scale applications, including hybrid electric vehicles (HEVs), electric vehicles (EVs) and stationary energy storage as well. However, the currently commercial graphite anode could not satisfy the requirement of high energy and power density for LIBs applied in the large-scale power storage. Transition metal oxides，especially Co_3O_4 and Fe_2O_3, are regarded as the most promising anode materials and have received extensive attention as a result of their excellent theoretical capacities and convenient synthesis, and they indeed exhibit superior electrochemical performance compared with graphite.[1-13] Recently, a series of Co-based ternary oxides, such as MCo_2O_4 (M = Ni. Zn, Cu), have been used as anode materials for LIBs and exhibit improved reversible capacities and enhanced cycling stability.[14-16] Despite of these progresses, the huge volume change, limited electron and Li^+ diffusion kinetics of metal oxides during the charge-discharge process, still impose restrictions on their commercial implementations. Therefore, exploiting anode materials towards high-capacity practical applications has been an urgent topic for the near future. One interesting strategy to improve the electrochemical performance of electrode materials is to assemble different oxides into a hierarchical composite, which could combine the unique properties of individual constituent and allow us to make use of their interaction for the better performance of the electrode materials.[17-21] Another promising route is to design electrode materials with hollow structure, which could effectively relieve the volume expansion and contraction of electrode materials during the charge-discharge process.[22-23] Thus, the electrochemical performance for LIBs might be enhanced by assembling different oxides into hollow nanocomposite.

Metal-organic frameworks (MOFs) with large surface areas, adjustable pore size and diverse skeleton structures are synthesized by assembling metal ion or metal clusters with organic ligands through coordination bond. MOFs have been regarded as multifunctional materials and hold promising in the applications of catalysis,[24-26] gas storage or separation,[27-29] sensoring,[30-32] and energy storgae.[33-35] Of all the MOFs, core-shell MOFs are particularly interesting and draw a great deal of attention.[36-38] The core-shell MOFs not only modify the porous properties of the core but also add new functions to the composite, resulting in the fabrication of multifunctional MOFs. One widely used way to synthesize core-shell MOFs is to epitaxial deposition of a different shell on the core MOFs and there have been some successful examples.[37,38] Nevertheless, the applications of core-shell MOFs are still in early stage.

Recently, some MOFs have been used as precursors to generate porous metal oxides through a thermal process.[39-41] Such porous structure is an effective strategy to relieve the stress of the electrode materials during the electrochemical reaction. In this regard, various metal oxides such as Fe_2O_3 nanoboxes,[42] agglomerated Co_3O_4 nanoparticles,[43] CuO/Cu_2O hollow polyhedrons,[44] *etc*., have been fabricated and exhibit promising electrochemical performance as anode materials for

LIBs. However, to the best of our knowledge, no research on synthesis of porous hollow nanocomposite from core-shell MOFs as anode materials for LIBs has been reported.

In this work, Fe_2O_3@$NiCo_2O_4$ porous nanocages have been successfully synthesized based on step-by-step MOFs growth and the subsequent annealing process. When evaluated as anode materials, the nanocomposite exhibits significantly enhanced specific capacity, rate capability and cycling performance.

Experimental

Synthesis of $Ni_3[Co(CN)_6]_2$ nanocubes

All chemicals used in this work were analytical grade and used without further purification. The typical synthetic experiments were carried out as follows: Solution A: 0.173 g of $NiCl_2$•$6H_2O$ and 1.234 g of sodium citrate were dissolved in 100 mL of distilled water with stirring to get a homogeneous solution. Solution B: 0.665 g of $K_3[Co(CN)_6]$ was dissolved in 100 mL of distilled water with stirring to form a clear solution. Solutions A and B were then mixed under magnetic stirring until the mixture became clear. After that, the reaction was aged at room temperature without any interruption for 10 h. The resulting pale-blue precipitation was centrifuged and washed several times with distilled water and absolute ethanol, and finally dried at room temperature for 12 h. The obtained powder was used as the seeds for the next step.

Synthesis of core-shell $Co_3[Fe(CN)_6]_2$@$Ni_3[Co(CN)_6]_2$ nanocubes

In a typical synthesis, [45, 46] 0.050 g of obtained seed, 0.390 g of $CoCl_2$•$6H_2O$ and 1.986 g of sodium citrate were dissolved in 100 mL water to form a dispersion in bottle A. In the meantime, 0.660 g of $K_3[Fe(CN)_6]$ was dissolved into 100 mL water to form a clear solution in bottle B. The solutions in bottles A and B were mixed under magnetic stirring until the mixture became clear. The obtained solution was aged for 24 h. Then the purple precipitates were collected by centrifugation. After extensive washing in water and ethanol, the purple precipitates were dried at room temperature. The obtained purple powder was $Ni_3[Co(CN)_6]_2$@$Co_3[Fe(CN)_6]_2$ particles with core-shell structure.

Preparation of $NiCo_2O_4$ nanocubes, Fe_2O_3@$NiCo_2O_4$ porous nanocages and the mixture of Fe_2O_3 and $NiCo_2O_4$

The $NiCo_2O_4$ nanocubes were synthesized by annealing $Ni_3[Co(CN)_6]_2$ at 450ºC for 6 h with a heating rate of 2ºC min^{-1}.

To convert the $Co_3[Fe(CN)_6]_2$@$Ni_3[Co(CN)_6]_2$ particles into Fe_2O_3@$NiCo_2O_4$ nanocages, the as-synthesized composite was heated in air at 450ºC for 6 h with a heating rate of 2ºC min^{-1}.

To make the mixture of Fe_2O_3 and $NiCo_2O_4$ (denoted as M-Fe_2O_3@$NiCo_2O_4$), the as-synthesized $NiCo_2O_4$ nanocubes were ball milled with Fe_2O_3 for 30 min and then annealed at 450ºC for 6 h with a heating rate of 2ºC min^{-1}.

Characterization

Powder X-ray diffraction (XRD) patterns were recorded by a Bruker D8 Focus and D/max 2500pc power X-ray diffractometer using Cu Kα radiation at a scan rate of 2° min^{-1}. Scanning electron microscope (SEM) images were performed on a Hitachi S-4800 field emission scanning electron microscope at an accelerating voltage of 10 kV. Transmission electron microscope (TEM), high-angle annular dark-field scanning transmission electron microscopy (HAADF-STEM) and element mapping were performed on a FEI Tecnai G2 S-Twin instrument with a field emission gun operating at 200 kV. Thermogravimetric (TG) curve was obtained on a STA 449ºC Jupiter (NETZSCH) thermogravimetry analyzer from 25 to 600ºC with a heating rate of 10ºC min^{-1}. N_2 adsorption-desorption measurements were conducted on a Micromeritics ASAP 2010 instrument at -196ºC with a pretreatment of the sample at 150ºC for 2 h under vacuum condition.

Electrochemical measurements

The working electrode was prepared by mixing the active materials, carbon black and poly(vinylidene fluoride) with a weight ratio of 50: 30: 20. Then N-methy1-2-pyrrolidone was added to the mixture to form homogeneous slurry and subsequently pressed on the Cu foil. The slurry coated copper foil was dried at 80ºC for 12 h. By using a pure lithium foil as the counter electrode, Celgard 2400 membrane as the separator, 1 M $LiPF_6$ dissolved in ethyl carbonate and diethyl carbonate (1:1, wt/wt) as the electrolyte, coin-type cells of 2025 were assembled in an glove box filled with highly pure argon gas. The charge-discharge performance was tested between 0.01-3.00 V using the LAND CT2001A multi-channel battery testing system at room temperature. The cyclic voltammogram (CV) measurement was conducted on a CHI660C Electrochemical Workstation at a scan rate of 0.1 mV s^{-1} in a potential range of 0.01-3 V *vs.* Li/Li^+.

Results and discussion

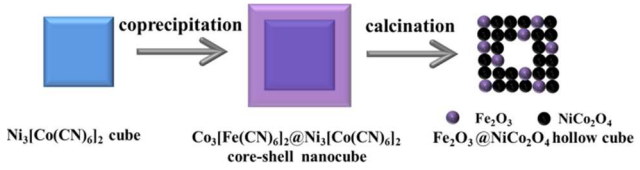

Fig. 1 Schematic of the procedure used to fabricate Fe_2O_3@$NiCo_2O_4$ porous nanocages.

The strategy to synthesize Fe_2O_3@$NiCo_2O_4$ porous nanocages is schematically depicted in Fig. 1. Prussian blue analogue (PBA) $Ni_3[Co(CN)_6]_2$ (NiCo) nanocubes are firstly fabricated by a coprecipitation method and used as the seeds for synthesizing heterogeneous structure. Due to the similar crystal structure

and lattice constant of Prussian blue analogues, it is possible to epitaxially deposit a layer of PB analogues to the seeds. Moreover, sodium citrate, which used as an additive, can interact with the metal ions dissolved in aqueous solution and slow down the coordination speed between metal ions and ligands, thereby decreasing the crystallization rate and leading to the second layer uniformly coating on the seeds. [47-50] As a result, a layer of $Co_3[Fe(CN)_6]_2$ (CoFe) deposits on the surface of NiCo nanocubes, forming a core-shell $Co_3[Fe(CN)_6]_2$@$Ni_3[Co(CN)_6]_2$ (CoFe@NiCo) nanocube structure. Eventually, the CoFe@NiCo precursor transforms to Fe_2O_3@$NiCo_2O_4$ nanocages after thermal treatment, which is mainly based on the nonequilibrium interdiffusion process. At the beginning of the calcination, the CoFe@NiCo precursor is not homogeneously heated, a high temperature gradient existing between the surface and the centre, which results in a thin layer of metal oxides forming on the surface of the CoFe@NiCo precursor. This thin layer with plenty of pores, can act as an interface to separate the inner CoFe@NiCo from the outside atmospheric oxygen and allow the outward diffusion of CoFe@NiCo through the pores. However, the diffusion rate of CoFe@NiCo is faster than that of atmospheric oxygen. Thus, a void space is generated between the thin layer and the unreacted CoFe@NiCo precursor. The volume loss and the release of the internally formed CO_2 and N_xO_y during the interdiffusion process eventually result in the formation of the hollow nanocages with porous shells.[39,42]

The formation of NiCo is confirmed by the XRD pattern (Supporting Information, Fig. S1), all the diffraction peaks can be assigned to $Ni_3[Co(CN)_6]_2$ with a cubic structure (space group Fm3m, a_0= 9.93 Å) and there are no impure phases existing. The strong intensity and narrow peak width indicate the NiCo with high crystallinity. The SEM images (Fig. S2) reveal the existence of a large amount of uniform NiCo nanocubes. The TEM images (Fig. S3) give that the nanocubes have smooth surface with an average size of 378 nm (Fig. S4 and Table S1). Fig. 2 shows the XRD characterisation of CoFe@NiCo particles. Considering that CoFe has similar structure and lattice constants to that of NiCo, their peak positions should be of little difference, so the XRD pattern in Fig. 2 is identical to the structure of CoFe, which has a face-center-cubic structure (space group F-43m, a_0=10.295 Å). Element mapping analysis is conducted to confirm the successful deposition of CoFe on the surface of NiCo. As shown in Fig. 3b, more Ni distributes in the center part than the edge part, while Fe mainly distributes on the edges and Co disperses evenly across the entire particle, indicating the formation of CoFe@NiCo core-shell structure. Fig. 3c shows that the synthesized CoFe@NiCo particles still keep a uniform cubic structure with smooth surface and the size is about 413 nm (Fig. S4 and Table S1). By comparing the TEM images of the NiCo (Fig. S3) with the CoFe@NiCo (Fig. 3d), it can be concluded that the CoFe@NiCo has a core-shell structure, which further confirms the deposition of CoFe on the surface of NiCo. Based on the above discussion, core-shell CoFe@NiCo nanocubes have been successfully fabricated through step-by-step coprecipitation method.

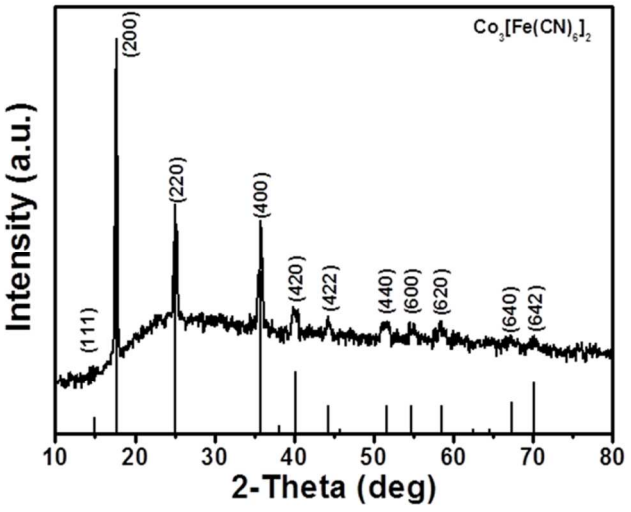

Fig. 2 XRD pattern of the as-prepared core-shell CoFe@NiCo nanocubes.

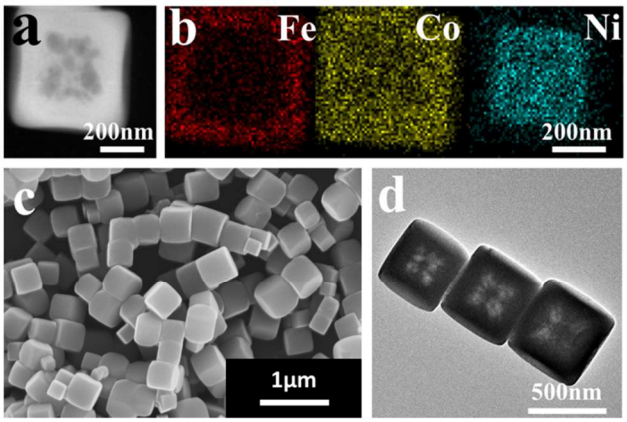

Fig. 3 (a) HAADF-STEM image (b) Elemental mappings (c) SEM image (d) TEM image of the core-shell CoFe@NiCo particles.

As shown in the TG curve of Fig. S5, there are two decomposition steps. The first step shows a weight loss of about 13.59 wt% between room temperature and 200 ℃, attributing to the loss of water molecule adsorbed in the structure. The second weight loss of about 16.09 wt% between 300ºC and 350ºC is due to the oxidation of CN^- to CO_2 and N_xO_y, which is accompanied with the decomposition of surfactant PVP. Based on the above TG result, 450ºC is chosen as the annealing temperature. The XRD pattern in Fig. 4 shows that the thermal product is composed of $NiCo_2O_4$ and Fe_2O_3 only, implying the successful synthesis of Fe_2O_3@$NiCo_2O_4$ composite. Fig. 5a and Fig. 5b reveal that the core-shell CoFe@NiCo nanocubes convert to nanocages with single shell. As can be seen in the element mapping of Fig. 5b, the Ni, Co and Fe all distribute on the edges of the particles, implying the homogeneous mixing of $NiCo_2O_4$ and Fe_2O_3. The SEM image

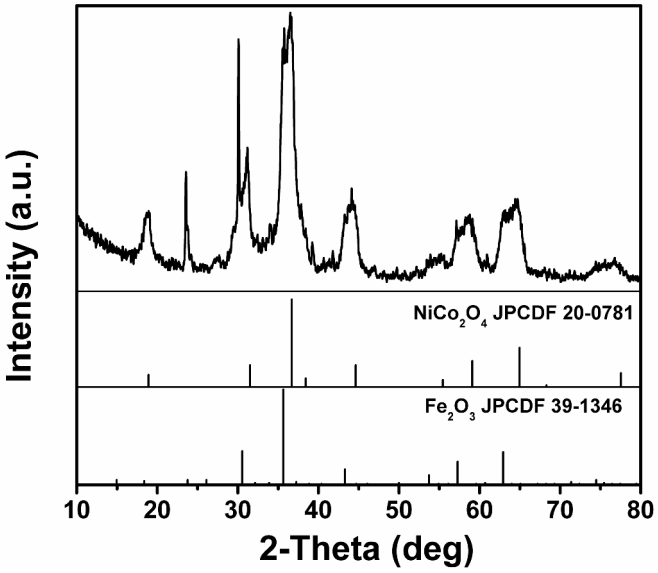

Fig. 4 XRD pattern of the as-prepared Fe_2O_3@$NiCo_2O_4$ nanocages.

in Fig. 5c exhibits that the obtained product maintains the cube morphology after thermal process except the surface becoming rough. Moreover, the broken particles in the SEM image disclose their hollow cube structure. The TEM image in Fig. 5d further confirms that the structure of Fe_2O_3@$NiCo_2O_4$ composite is nanocage with single shell and the shell is composed by nanoparticles with size of several nanometers. The size of the Fe_2O_3@$NiCo_2O_4$ nanocubes is about 213 nm (Fig. S4 and Table S1) and the shell thickness is approximately to 35 nm. The difference in size between the initial core-shell crystals of PBA and the final oxide composite is mainly contributed to the remove of C-N parts by calcination and the difference in unit cell parameters.

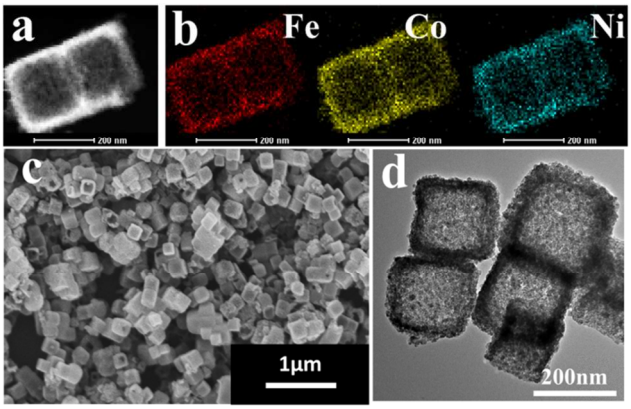

Fig. 5 (a) HAADF-STEM image (b) Elemental mappings (c) SEM image (d) TEM image of Fe_2O_3@$NiCo_2O_4$ nanocages.

To characterize the specific surface areas and pore-size distribution of Fe_2O_3@$NiCo_2O_4$ nanocages, N_2 adsorption-desorption analysis has been conducted at -196ºC and the results are shown in Fig. S6a. The sorption isotherms are of type IV isotherm with a H2-type hysteresis loop over the range of $0.7 < P/P_0 < 0.98$, indicating the mesopores characteristic. The Fe_2O_3@$NiCo_2O_4$ nanocages have a BET surface area of 12.72 m^2 g^{-1} and the total pore volume is 0.083 cm^3 g^{-1}. A BJH calculation based on adsorption data gives the pore size distribution, which has a bimodal distribution with a narrow distribution centring at 10.3 nm and a wide distribution centring at 18.4 nm. The average pore size centres at 18.67 nm (Fig. S6b). These mesoporous not only provide interconnected paths for electrolyte, Li^+ and electrons transport, but also buffer the huge volume change of the electrode materials during the repeated charge-discharge process.

To evaluate the electrochemical performance of Fe_2O_3@$NiCo_2O_4$ nanocages as anode materials for LIBs, the CV and charge–discharge measurements have been conducted. Fig. 6a shows the first three CV curves of Fe_2O_3@$NiCo_2O_4$ nanocages at a scan rate of 0.1 mV s^{-1} in the potential range of 0.01-3 V *vs.* Li/Li^+. The intense peak at 1.72 V in the first cathodic sweep corresponds to the reduction of Ni^{2+}, Co^{2+}, Co^{3+} and Fe^{3+} to metallic Ni, Co and Fe. In the subsequent cycles, the main cathodic peak shifts to 0.85 V, indicating that the latter reduction mechanism is different from the first one. The small peak at 1.45 V might be ascribed to partial reduction of Fe^{3+} to Fe^{2+}. During the anodic process, the peak at 1.60 V attributes to the oxidation of Ni to Ni^{2+} and Fe to Fe^{3+}, while the peak at 2.15 V corresponds to the oxidation of Co to Co^{3+}. Apart from the first cycle, the subsequent cycles overlap well, indicating the superior reversibility of the electrochemical reaction. Based on the CV result, ex XRD patterns of the Fe_2O_3@$NiCo_2O_4$ electrode (Fig. S7) and the storage mechanisms of $NiCo_2O_4$ and Fe_2O_3,[51-55] the whole electrochemical reactions are believed to be as follows:

$$NiCo_2O_4 + 8Li^+ + 8e^- \rightarrow Ni + 2Co + 4Li_2O \quad (1)$$

$$Ni + Li_2O \leftrightarrow NiO + 2Li^+ + 2e^- \quad (2)$$

$$2Co + 2Li_2O \leftrightarrow 2CoO + 4Li^+ + 4e^- \quad (3)$$

$$2CoO + 2/3Li_2O \leftrightarrow 2/3Co_3O_4 + 4/3Li^+ + 4/3e^- \quad (4)$$

$$Fe_2O_3 + 6Li^+ + 8e^- \leftrightarrow 2Fe + 3Li_2O \quad (5)$$

Representative charge-discharge voltage profiles for the 1st, 2nd, 10th, 50th and 100th cycles of the Fe_2O_3@$NiCo_2O_4$ nanocages electrode at the current density of 100 mA g^{-1} (about 0.1 C) are shown in Fig. 6b. There is a long flat discharge voltage plateau at about 0.85 V in the first cycle, which then gradually decreases to 0.01 V. The flat plateau is replaced by a sloping curve after the first cycle due to the heterogeneous reaction mechanism between Li and the electrode materials, which is consistent with the CV results. The initial discharge and charge capacities are 1311.4 and 902.7 mAh g^{-1}, respectively. The large irreversible capacity loss in the initial cycle could be attributed to the formation of the solid electrolyte interface

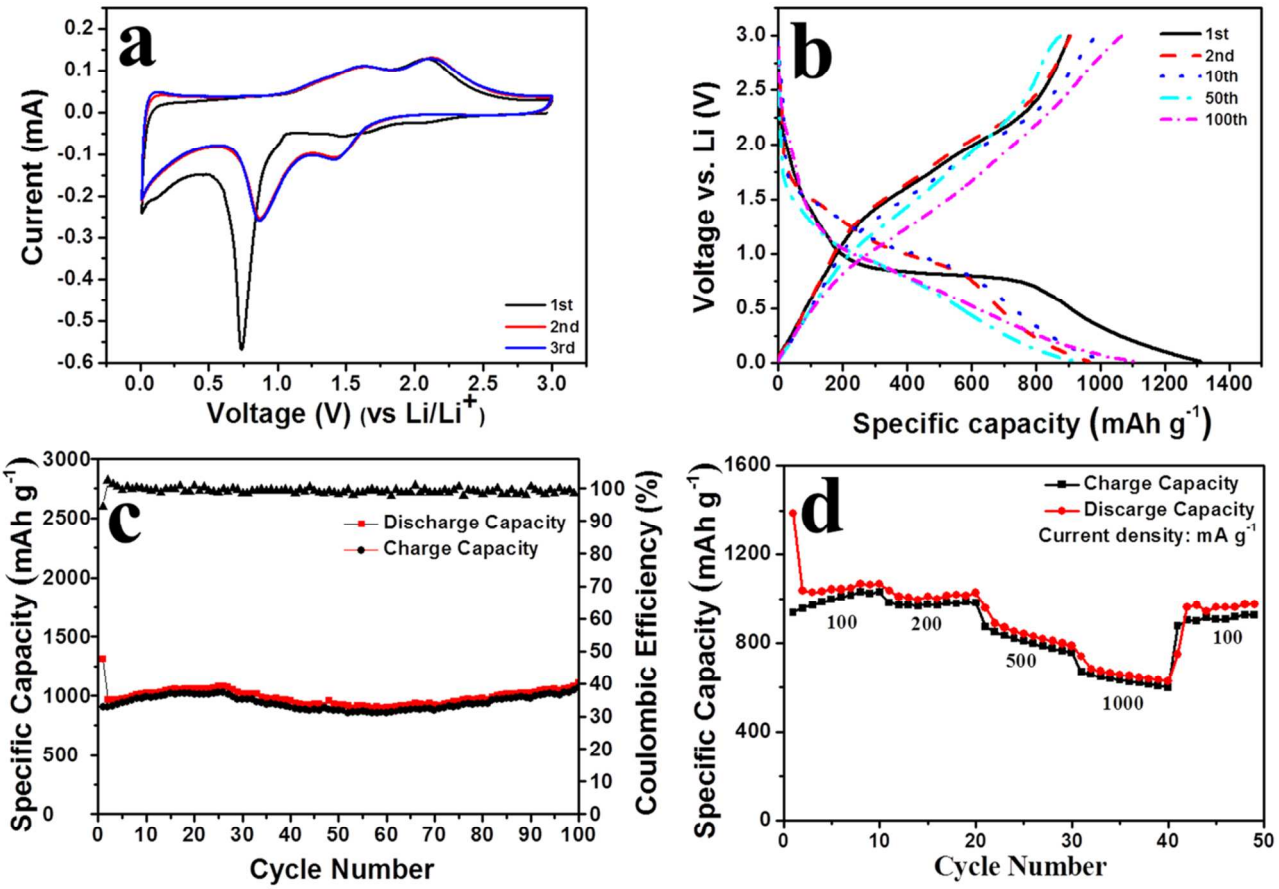

Fig. 6 (a) Representative cyclic voltammograms (CVs) of the Fe_2O_3@$NiCo_2O_4$ nanocages at a scan rate of 0.1 mV s^{-1} between 0.01 and 3 V *vs.* Li/Li^+. (b) Charge–discharge voltage profiles of the Fe_2O_3@$NiCo_2O_4$ nanocages for the 1st, 2nd, 10th, 50th and 100th cycles in the voltage range of 0.01 - 3.0 V at a current rate of 100 mA g^{-1} (0.1 C). (c) Capacity and coulombic efficiency *vs*. cycle number of the Fe_2O_3@$NiCo_2O_4$ nanocages at a current rate of 100 mA g^{-1} (0.1 C). (d) Rate capability of the Fe_2O_3@$NiCo_2O_4$ nanocages anode.

(SEI) film and irreversible decomposition of the electrolyte.[56] The 2nd, 10th, 50th and 100th discharge capacities of Fe_2O_3@$NiCo_2O_4$ electrode are 906.4, 1013.4, 931.2 and 1079.6 mAh g^{-1}, separately. In the case of $NiCo_2O_4$ electrode, the measured 1st, 2nd, 10th, 50th and 100th discharge capacities are 1494.8, 1095.1, 952.8, 453.1 and 274.6 mAh g^{-1}, separately (Fig. S8a). It is notable that the capacity retention for the Fe_2O_3@$NiCo_2O_4$ electrode is much better than that of $NiCo_2O_4$ electrode.

The cycling performance of the Fe_2O_3@$NiCo_2O_4$ nanocages is depicted in Fig. 6c. It indicates that during the whole charge-discharge process, the discharge capacity of the Fe_2O_3@$NiCo_2O_4$ is stable at around 1000 mAh g^{-1}, while the capacities of $NiCo_2O_4$ and M-Fe_2O_3@$NiCo_2O_4$ electrodes decay rapidly, which are only 274.6 and 214.7 mAh g^{-1} after 100 cycles (Fig. S8b and Fig. S8c). Furthermore, from the second cycle onward, the Coulombic efficiency of the Fe_2O_3@$NiCo_2O_4$ nanocages is above 96%, indicating the excellent capacity retention of the composite electrode. To make the electrochemical measurement more convince, the ratio of the active materials, acetylene black and PVDF is changed from 50:30:20 to 70:20:10 and the result is shown in Fig. S8d. It reveals that the Fe_2O_3@$NiCo_2O_4$ (7:2:1) anode exhibits stable capacity retention and a discharge capacity of 904.1 mAh g^{-1} could still be maintained after 100 charge-discharge cycles at the current density of 200 mA g^{-1}. The cycling stability is almost with no obvious change after changing the ratio of the active materials.

Fig. 6d gives the multiple-step galvanostatic charge-discharge results of the Fe_2O_3@$NiCo_2O_4$ nanocages. The cells exhibit good rate performance with average discharge capacities of 1083.5, 1015.1, and 846.5 mAh g^{-1} at current density of 100, 200 and 500 mA g^{-1} (0.1, 0.2 and 0.5 C), separately. Even at the current density of 1000 mA g^{-1} (1 C), the discharge capacity could still retains 661.8 mAh g^{-1}, which is far exceeding the capacity of the graphite at such high current density with the same voltage range of 0.01-3 V *vs.* Li/Li^+. Importantly, the discharge capacity recovers to 944.7 mAh g^{-1} when the current density returns to 100 mA g^{-1} (0.1 C).

The enhanced specific capacity, rate capability and cycling performance of Fe_2O_3@$NiCo_2O_4$ nanocages can be attributed to the following factors. Firstly, both the hollow structure and the porous shell architecture could allow better intercalation of Li^+ in the electrode, accelerate their diffusion velocity and shorten

the Li^+ diffusion length. Also, the porous hollow structure increases the electrolyte/active materials contact area and reduces the resistance of electrolyte penetration. Secondly, the numerous pores could partially relax the stress caused by volumetric expansion and contraction during Li uptake and removal. Furthermore, during the charge-discharge process, the different phases react with lithium at different potentials, so the volume expansion and contraction of the composite electrode is happened sequentially, thus efficiently tune the stress and alleviate the structure pulverization during cycling. Finally, the interaction of the Fe_2O_3 and $NiCo_2O_4$ and the combination of the unique properties of individual constituent may also contribute to the better electrochemical performance.[21, 42]

Conclusions

In summary, this work reports the synthesis of Fe_2O_3@$NiCo_2O_4$ porous nanocages with nanometer-sized building blocks by using core-shell MOFs as template. The Fe_2O_3@$NiCo_2O_4$ nanocages exhibit high capacity, excellent cycling stability and rate capability when used as anode materials for LIBs. The improved electrochemical performance is ascribed to the hierarchical porous hollow structure and the homogeneous mixing of Fe_2O_3 and $NiCo_2O_4$. Furthermore, this strategy is quite versatile and can be extended to synthesize other novel materials by using MOFs as template.

Acknowledgement

This work is supported by the National Nature Science Foundation of China （Grant No. 20111061）.

Notes and references

[a] *State Key Laboratory of Rare Earth Resource Utilization, Changchun Institute of Applied Chemistry, CAS, Changchun, 130022, China. Email: lmwang@ciac.ac.cn, Tel: +86-431-85262447, Fax: +86-431-85262836;*
[b] *Changzhou Institute of Energy Storage Materials and Devices, Changzhou 213000, China.*
[c] *University of Chinese Academy of Sciences, Beijing 100049, China.*

Electronic Supplementary Information (ESI) available: detailed supplementary figures. See DOI: 10.1039/b000000x/

1 J. M. Tarascon and M. Armand, *Nature*, 2001, **414**, 359.
2 Y. G. Zhu, J. Xie, G. S. Cao, T. J. Zhu and X. B. Zhao, *RSC Adv*., 2013, **3**, 6787.
3 X. H. Xia, J. P. Tu, Y. Q. Zhang, J. Chen, X. L. Wang, C. D. Gu, C. Guan, J. S. Luo and H. J. Fan, *Chem. Mater*., 2012, **24**, 3793.
4 L. L. Wang, J. W. Liang, Y. C. Zhu, T. Mei, X. Zhang, Q. Yang and Y. T. Qian, *Nanoscale*, 2013, **5**, 3627.
5 F. F. Xia, X. L. Hu, Y. M. Sun, W. Luo and Y. H. Huang, *Nanoscale*, 2012, **4**, 4707.
6 Y. Q. Zou and Y. Wang, *Nanoscale*, 2011, **3**, 2615.
7 Y. J. Mai, J. P. Tu, X. H. Xia, C. D. Gu and X. L. Wang, *J. Power Sources*, 2011, **196**, 6388.
8 J. Chen, X. H. Xia, J. P. Tu, Q. Q. Xiong, Y. X. Yu, X. L. Wang and C. D. Gu, *J. Mater. Chem*., 2012, **22**, 15056.
9 Q. Q. Xiong, J. P. Tu, Y. Lu, J. Chen, Y. X. Yu, X. L. Wang and C. D. Gu, *J. Mater. Chem*., 2012, **22**, 18639.
10 X. L. Huang, R. Z. Wang, D. Xu, Z. L. Wang, H. G. Wang, J. J. Xu, Z. Wu, Q. C Liu, Y. Zhang and X. B. Zhang, *Adv. Funct. Mater*., 2013, **23**, 4345.
11 Z. Y. Wang, L. Zhou and X. W. Lou, *Adv. Mater*., 2012, **24**, 1903.
12 H. B. Wu, J. S. Chen, H. H. Hng and X. W. Lou, *Nanoscale*, 2012, **4**, 2526.
13 C. Z. Yuan, H. B. Wu, Y. Xie and X. W. Lou, *Angew. Chem. Int. Ed*., 2013, **DOI**: 10.1002/anie.201303971.
14 L. L. Li, Y. L. Cheah, Y. Ko, P. F. Teh, G. Wee, C. Wong, S. J. Peng and M. Srinivasan, *J. Mater. Chem. A*, 2013, **1**, 10935.
15 J. F. Li, J. Z. Wang, D. Wexler, D. Q. Shi, J. W. Liang, H. K. Liu, S. L. Xiong and Y. T. Qian, *J. Mater. Chem. A*, 2013, **DOI:** 10.1039/C3TA13787B.
16 Y. Sharma, N. Sharma, G. V. Subba Rao and B. V. R. Chowdari, *Adv. Funct. Mater*., 2007, **17**, 2855.
17 H. Wu, M. Xu, Y. C. Wang and G. F. Zheng, *Nano Res*., 2013, **6**, 167.
18 Y. S. Luo, J. S. Luo, W. W. Zhou, X. Y. Qi, H. Zhang, D. Y. Yu, C. M. Li, H. J. Fan and T. Yu, *J. Mater. Chem. A*, 2013, **1**, 273.
19 N. A. Kyerematen, C. Lebouin, P. Knauth and T. Djenizian, *Electrochim. Acta*, 2013, **88**, 814.
20 X. H. Xia, J. P. Tu, Y. Q. Zhang, X. L. Wang, C. D. Gu, X. B. Zhao and H. J. Fan, *ACS Nano*, 2012, **6**, 5531.
21 M. M. Rahman, A. M. Glushenkov, T. Ramireddy, T. Tao and Y. Chen, *Nanoscale*, 2013, **5**, 4910.
22 X. Wang, X. L. Wu, Y. G. Guo, Y. T. Zhong, X. Q. Cao, Y. Ma and J. N. Yao, *Adv. Funct. Mater*., 2010, **20**, 1680.
23 J. M. Jeong, B. G. Choi, S. C. Lee, K. G. Lee , S. J. Chang, Y. K. Han, Y. B. Lee, H. U. Lee, S. Kwon, G. Lee, C. S. Lee and Y. S. Huh, *Adv. Mater*., 2013, **DOI:** 10.1002/adma.201302710.
24 J. Y. Lee, O. M. Farha, J. Roberts, K. A. Scheidt, S. T. Nguyen and J. T. Huppal, *Chem. Soc. Rev*., 2009, **38**, 1450.
25 Q. L. Zhu, J. Li and Q. Xu, *J. Am. Chem. Soc.*, 2013, **135**, 10210.
26 M. Yoon, R. Srirambalaji and K. Kim, *Chem. Rev*., 2012, **112**, 1196.
27 N. L. Rosi, J. Eckert, M. Eddaoudi, D. T. Vodak, J. Kim, M. O'Keeffe and O. M. Yaghi, *Science*, 2003, **300**, 1127.
28 L. Ge, W. Zhou, V. Rudolph and Z. H. Zhu, *J. Mater. Chem. A*, 2013, **1**, 6350.
29 P. Ju, L. Jiang and T. B. Lu, *Chem. Commun*., 2013, **49**, 1820.
30 M. D. Allendorf, C. A. Bauer, R. K. Bhakta and R. J. T. Houk, *Chem. Soc. Rev*., 2009, **38**, 1330.
31 L. E. Kreno, K. Leong, O. K. Farha, M. Allendorf, R. P. Van Duyne and J. T. Hupp, *Chem. Rev*., 2012, **112**, 1105.
32 J. W. Cao, Y. F. Gao, Y. Q. Wang, C. F. Dua and Z. L. Liu, *Chem. Commun*., 2013, **49**, 6897.
33 G. Combarieu, M. Morcrette, F. Millange, N. Guillou, J. Cabana, C. P. Grey, I. Margiolaki, G. Ferey and J. M. Tarascon, *Chem. Mater*., 2009, **21**, 1602.
34 A. Morozan and F. Jaouen, *Energy Environ. Sci*., 2012, **5**, 9269.
35 S. L. Lia and Q. Xu, *Energy Environ. Sci*., 2013, **6**, 1656.
36 A. Gehin, S. Ferlay, J. M. Harrowfield, D. Fenske, N. Kyritsakas and M. W. Hosseini, *Inorg. Chem.,* 2012, **51**, 5481.
37 S. H. Furukawa, K. J. Hirai, K. J. Nakagawa, Y. H. Takashima, R. Matsuda, T. Tsuruoka, M. Kondo, R. Haruki, D. Tanaka, H.

Sakamoto, S. Shimomura, O. Sakata and S. Kitagawa, *Angew. Chem. Int. Ed*., 2009, **48**, 1766.
38 K. Koh, A. G. W. Foy and A. J. Matzger, *Chem. Commun*., 2009, 6162.
39 L. Hu, N. Yan, Q. W. Chen, P. Zhang, H. Zhong, X. R. Zheng, Y. Li and X. Y. Hu, *Chem. Eur. J*., 2012, **18**, 8971.
40 F. L. Meng, Z. G. Fang, Z. X. Li, W. W. Xu, M. J. Wang, Y. P. Liu, X. N. Qu, W. R. Wang, D. Y. Zhao and X. H. Guo，*J. Mater. Chem. A*, 2013, **1**, 7235.
41 T. K. Kim, K. J. Lee, J. Y. Cheon, J. H. Lee, S. H. Joo and H. R. Moon, *J. Am. Chem. Soc*., 2013, **135**, 8940.
42 L. Zhang, H. B. Wu, S. Madhavi, H. G. Hng and X. W. Lou, *J. Am. Chem. Soc*., 2012, **134**, 17388.
43 B. Liu, X. B. Zhang, H. Shioyama, T. Mukai, T. Sakai and Q. Xu, *J. Power Sources*, 2010, **195**, 857.
44 L. Hu, Y. M. Huang, F. P. Zhang and Q. W. Chen, *Nanoscale*, 2013, **5**, 4186.
45 L. Zhang, H. B. Wu and X. W. Lou, *J. Am. Chem. Soc*., 2013, **135**, 10664.
46 P. Nie, L. F. Shen, H. F. Luo, H. S. Li, G. Y. Xu and X. G. Zhang, *Nanoscale*, 2013, **DOI**: 10.1039/C3NR03289B.
47 L. Catala, D. Brinzei, Y. Prado, A. Gloter, O. Stéphan, G. Rogez and T. Mallah, *Angew. Chem, Int. Ed*., 2009, **48**, 183.
48 M. F. Dumont, E. S. Knowles, A. Guiet, D. M. Pajerowski, A. Gomez, S. W. Kycia, M. W. Weisel and D. R. Talham, *Inorg. Chem*., 2011, **50**, 4295.
49 N. Kotsakis, C. P. Raptopoulou, V. Tangoulis, A. Terzis, J. Giapintzakis, T. Jakusch, T. Kiss and A. Salifoglou, *Inorg. Chem*., 2003, **42**, 22.
50 M. Matzapetakis, N. Karligiano, A. Bino, M. Dakanali, C. P. Raptopoulou, V. Tagoulis, A. Terzis, J. Giapintzakis and A. Salifoglou, *Inorg. Chem*., 2000, **39**, 4044.
51 J. F. Li, S. L. Xiong, Y. R. Liu, Z. C. Ju and Y. T. Qian, *Appl. Mater. Interfaces*, 2013, **5**, 981.
52 Y. J. Chen, B. H. Qu, L. L. Hu, Z. Xu, Q. H. Li and T. H. Wang, *Nanoscale*, 2013, **5**, 9812.
53 R. G. Ma, L. F. He, Z. G. Lu, S. L. Yang, L. J. Xia and C. Y. Chung, *CrystEngComm*., 2012, **14**, 7882.
54 Z. Y. Wang, D. Y. Luan, S. Madhavi, C. M. Lia and X. W. Lou, *Chem. Commun*., 2011, **47**, 8061.
55 M. Y. Son, Y. J. Hong, J. K. Lee and Y. C. Kang, *Nanoscale*, 2013, **DOI:** 10.1039/C3NR03978A.
56 Z. Wang, D. Luan, S. Madhavi, Y. Hu, X. W. Lou, *Energy Environ. Sci.* 2012, **5**, 5252.